Composite Structures 330 (2024) 117696

Contents lists available at ScienceDirect

Composite Structures

journal homepage: www.elsevier.com/locate/compstruct

An enhanced constitutive model to predict plastic deformation and multiple failure mechanisms in fibre-reinforced polymer composite materials

I.R. Cózar [a,*], F. Otero [b,c], P. Maimí [a], E.V. González [a], A. Turon [a], P.P. Camanho [d,e]

[a] AMADE, Polytechnic School, University of Girona, Campus Montilivi s/n, 17071 Girona, Spain
[b] CIMNE, Universitat de Politècnica de Catalunya, 08034 Barcelona, Spain
[c] Department of Nautical Science and Engineering, Universitat Politècnica de Catalunya, Pla de Palau 18, 08003 Barcelona, Spain
[d] DEMec, Faculdade de Engenharia, Universidade do Porto, 4200-465 Porto, Portugal
[e] INEGI, Instituto de Ciência e Inovação em Engenharia Mecânica e Industrial, 4200-465 Porto, Portugal

ARTICLE INFO

Keywords:
Computational modelling
Damage mechanics
Plastic deformation
Numerical analysis
Spurious damage

ABSTRACT

Spurious damage modes in continuum damage mechanics models for fiber-reinforced polymer composite materials based on the effective stress tensor can be generated when large strains occur. A methodology to prevent this spurious phenomenon is developed in the present work. The longitudinal damage activation functions are based on the effective stress tensor, however, nominal stresses are used on the transverse damage activation functions. The proposed method can be straightforwardly implemented on previously-developed constitutive models which use the effective stress tensor, an explicit implementation of the proposed constitutive model is presented. The enhancement of the predicted failure mechanisms obtained from the present constitutive model, with respect to the models which use the effective stress tensor, is demonstrated. The proposed constitutive model presents a good agreement of the predicted failure pattern obtained from open-hole compressive experimental tests, as well as on the predicted failure strength.

1. Introduction

Fibre-reinforced polymer (FRP) composite materials present different failure mechanisms such as fibre failure, matrix cracking, delamination and buckling, due to their complex manufacturing process and mechanical behaviour [1]. Fibre failure under tensile loading occurs on a plane perpendicular to the longitudinal axis, whereas compressive fibre failure is due to the collapse of the fibres and promotes shear kinking and matrix damage [2,3]. Matrix cracking occurs in the resin, accounting for fibre-matrix debonding or voids. Delamination between layers is promoted by interlaminar stresses that develop at the free edges.

Continuum damage mechanics (CDM) theory is often employed in conjunction with finite element (FE) models to predict crack initiation and propagation in FRP composite materials [1,4,5]. CDM models represent a crack by introducing damage variables (d_M) in the corresponding terms of the elasticity tensor ($\mathbb{C}_e(d_M)$) to obtain the stress tensor ($\boldsymbol{\sigma}$) as a function of the elastic strain tensor ($\boldsymbol{\varepsilon}^e$),

$$\boldsymbol{\sigma} = \mathbb{C}_e(d_M)\boldsymbol{\varepsilon}^e. \tag{1}$$

Therefore, the non-linear response due to cracking is obtained without explicitly modelling it in the mesh.

The terms of $\mathbb{C}_e$ are often modified according to the corresponding d_M obtained from a failure criterion. For example, Maimí et al. [6] modelled a longitudinal crack resulting from tensile stresses by reducing the longitudinal Young's modulus as a function of a damage variable obtained from the non-interactive maximum strain failure criterion. The authors evaluated the failure criterion using the effective stress tensor ($\tilde{\boldsymbol{\sigma}}$). This framework was introduced by Lemaitre [7] and is based on the *hypothesis of Strain Equivalence* [7,8]. The hypothesis considers that the strain associated to a damaged stress state ($\boldsymbol{\sigma}$) is equivalent to the strain associated with its effective stress state (undamaged stress state, $\tilde{\boldsymbol{\sigma}}$). The effective stress tensor can be calculated as a function of the elastic material properties and $\boldsymbol{\varepsilon}^e$ as

$$\tilde{\boldsymbol{\sigma}} = \mathbb{C}_e(d_M = 0)\boldsymbol{\varepsilon}^e, \tag{2}$$

and is widely used to evaluate the failure criteria in CDM models [5,6,9–16]

One of the main advantages of using $\tilde{\boldsymbol{\sigma}}$ in CDM models is to develop a constitutive model efficient in terms of computational time. The elastic material properties (i.e., $\mathbb{C}_e(d_M = 0)$) and $\boldsymbol{\varepsilon}^e$ are the known data in CDM models with $\tilde{\boldsymbol{\sigma}}$ while evaluating the failure criteria. Therefore, the damage only depends on the strain tensor and can be explicitly

* Corresponding author.
E-mail address: ivan.ruiz@udg.edu (I.R. Cózar).

https://doi.org/10.1016/j.compstruct.2023.117696
Received 27 March 2023; Received in revised form 1 August 2023; Accepted 2 November 2023
Available online 18 December 2023

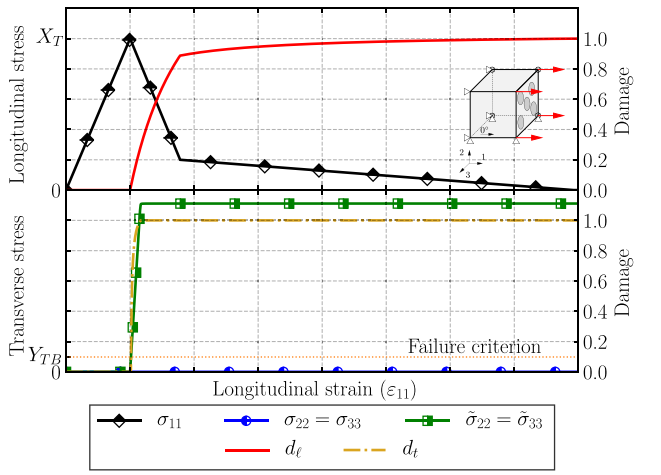

Fig. 1. Longitudinal virtual tensile test at the Gauss-point level using a CDM model based on $\tilde{\boldsymbol{\sigma}}$, where d_ℓ and d_t are the damage variables associated to the longitudinal and transverse direction, respectively, X_T is the longitudinal tensile strength and Y_{TB} is the biaxial transverse tensile strength. (Top) Longitudinal response, and (bottom) transverse response.

found. However, an iterative implicit solution for the damage variables should be employed in CDM models which use $\boldsymbol{\sigma}$ to evaluate the failure criteria [17–20], then the computational time increases.

The use of $\tilde{\boldsymbol{\sigma}}$ in evaluating failure criteria can induce the activation of damage variables corresponding to failure mechanisms that should not occur [21]. A large elastic strain in a particular direction due to damage produces a large effective stress in that direction, but also large effective stresses in other directions may be generated. This phenomenon is observed in the pure longitudinal and transverse directions of $\tilde{\boldsymbol{\sigma}}$, due to the coupling of the strains by the Poisson's ratios. For example, a uniaxial loading in the longitudinal direction activates damage variables associated to the longitudinal direction (d_ℓ). This longitudinal damage produces effective stresses in the pure transverse directions,

$$\tilde{\sigma}_{22} = \tilde{\sigma}_{33} = \frac{E_{11} E_{22} \nu_{12}}{E_{11}(1-\nu_{23}) - 2E_{22}\nu_{12}^2} d_\ell \varepsilon_{11}^e, \tag{3}$$

where E_{11} and E_{22} are the Young's modulus in longitudinal and transverse direction, respectively, and ν_{12} and ν_{23} are the longitudinal and transverse Poisson's ratios, respectively. Hence, damage variables associated to the transverse directions can be activated despite the nominal stresses being null ($\sigma_{22} = \sigma_{33} = 0$), see Fig. 1. Consequently, spurious damage can be generated in the transverse directions. This event is a general limitation of constitutive models which use $\tilde{\boldsymbol{\sigma}}$. This phenomenon can be observed in the literature constitutive models [6,11,13,15,16].

Matzenmiller et al. [10] proposed a damage model to describe the mechanical behaviour of FRP composite materials based on the CDM theory. The model described four failure mechanisms: (i) fibre failure due to traction; (ii) fibre buckling and kinking due to compression; (iii) matrix cracking under transverse tension and shearing; and (iv) matrix cracking under transverse compression and shearing. Each failure mechanism listed above was associated with a failure criterion as a function of $\tilde{\boldsymbol{\sigma}}$ and its corresponding damage variable. The authors avoided the coupling of the components of $\tilde{\boldsymbol{\sigma}}$ when the damage is achieved by degrading the Poisson's ratios as a function of the corresponding damage variable. These relationships were assumed from experimental evidence. This procedure allows the components of $\tilde{\boldsymbol{\sigma}}$ to be decoupled when damage occurs. Hence, the Poisson's ratios are a function of the damage variables that are unknown while $\tilde{\boldsymbol{\sigma}}$ must be calculated. Therefore, an iterative algorithm should be implemented to solve the model [22], thus increasing the computational time. In addition, the solution presented by Matzenmiller et al. [10] cannot be straightforwardly implemented in the previously developed constitutive models which use $\tilde{\boldsymbol{\sigma}}$ (e.g. the evolution of the damage variables must be redefined).

The main objective of this work is to present an improved approach to avoid spurious damage in CDM models which use $\tilde{\boldsymbol{\sigma}}$ due to large strains caused by damage in other directions. The solution presented here can be explicitly implemented in existing CDM models that have already been developed using $\tilde{\boldsymbol{\sigma}}$ [6,11,13,15,16] and linked with an explicit FE solver. The constitutive model presented by Cózar et al. [23], which is a 3D elastoplastic damage model based on CDM theory using $\tilde{\boldsymbol{\sigma}}$, is used as a baseline to demonstrate how the formulation of existing CDM models can be modified to avoid spurious damage modes developing.

The formulation of the constitutive model is presented in Section 2 and its implementation in a FE explicit solver in Section 3. A pure longitudinal virtual test at the Gauss-point level presented in Section 4 demonstrates that no spurious damage is found in the present constitutive model. In addition, open-hole compressive (OHC) tests with a multidirectional laminate and with unidirectional laminates are used to explain and demonstrate the improvement in the failure pattern predicted by the present model. Finally, the main conclusions are presented in Section 5.

2. Constitutive model

2.1. Complementary free energy and plastic evolution

The constitutive model used in this work is based on the elastoplastic damage model developed by Cózar et al. [23]. The additive decomposition of the infinitesimal strain tensor is assumed as

$$\boldsymbol{\varepsilon} = \boldsymbol{\varepsilon}^e + \boldsymbol{\varepsilon}^p, \tag{4}$$

where $\boldsymbol{\varepsilon}^e$ contains the cracking strains and $\boldsymbol{\varepsilon}^p$ is the plastic strain tensor. For homogenised composite materials, an elastic behaviour until the onset of plasticity in the directions governed by the matrix is assumed. Then, the plastic strains can grow until a matrix crack is started. After that, the damage develops without increasing the plastic strains at the Gauss-point level. However, plasticity is not considered in the longitudinal direction. The model describes a purely elastic response before the onset of damage in the longitudinal direction,.

The complementary Gibbs free-energy density function reads

$$\begin{aligned} W := & \frac{\sigma_\ell^2}{2(1-d_\ell)E_{11}} - \frac{2\nu_{12}\sigma_\ell p_t}{E_{11}} + \frac{p_t^2}{2(1-d_t)E_t} + \frac{\tau_t^2}{2(1-d_{st})G_t} \\ & + \frac{\tau_\ell^2}{2(1-d_{s\ell})G_{12}} + \boldsymbol{\sigma}\boldsymbol{\varepsilon}^p, \end{aligned} \tag{5}$$

where G_{12} is the longitudinal shear Young's modulus. E_t and G_t are the bulk and shear elastic stiffness, respectively, in the transverse isotropic plane which are defined as

$$E_t := \frac{E_{22}}{2(1-\nu_{23})} \tag{6}$$

and

$$G_t := \frac{E_{22}}{2(1+\nu_{23})}. \tag{7}$$

W depends on four of the five invariants of $\boldsymbol{\sigma}$ at a rotation with respect to the longitudinal axis: σ_ℓ related to the longitudinal stress component,

$$\sigma_\ell = \sigma_{11}; \tag{8}$$

p_t that describes the transverse hydrostatic pressure,

$$p_t = \frac{\sigma_{22} + \sigma_{33}}{2}; \tag{9}$$

τ_ℓ related to the longitudinal shear stresses,

$$\tau_\ell = \sqrt{\sigma_{12}^2 + \sigma_{13}^2}; \tag{10}$$

and τ_t related to the transverse shear stresses,

$$\tau_t = \frac{\sqrt{(\sigma_{22} - \sigma_{33})^2 + 4\sigma_{23}^2}}{2}, \tag{11}$$

where σ_{ij} are the Cartesian components of $\boldsymbol{\sigma}$.

Finally, the strain tensor is obtained applying the Clausius–Duhem inequality [9,24] as

$$\boldsymbol{\varepsilon} = \frac{\partial W}{\partial \boldsymbol{\sigma}} = \mathbb{H}\boldsymbol{\sigma} + \boldsymbol{\varepsilon}^p, \tag{12}$$

where $\mathbb{H}$ is the compliance tensor. In addition, four damage variables d_M ($M = \ell, t, s\ell, st$) are defined in W to describe the following failure mechanisms: d_ℓ associated to the longitudinal tensile failure ($\sigma_\ell > 0$) and the longitudinal compressive failure ($\sigma_\ell < 0$); d_t describes the mode-I matrix cracking; d_{st} associated to the mode-II matrix cracking; and $d_{s\ell}$ combines the longitudinal tensile and matrix failure mechanisms. Subscript ℓ refers to longitudinal, subscript t to transverse and subscript s to shear.

Regarding to the plasticity modelling, the model presented by Cózar et al. [23] is employed. The yield function is defined as

$$\begin{aligned}\phi^p(\boldsymbol{\sigma}, \bar{\varepsilon}^p) := &\sqrt{\left(\frac{Y_{CP} + Y_{TP}}{Y_{CP}Y_{TP}}\right)^2 \frac{\tau_t^2 + \mu_{tp}p_t^2}{1 + \mu_{tp}} + \left(\frac{\mu_{s\ell p}}{S_{LP}}\tau_\ell\right)^2} \\ &+ \frac{Y_{CP} - Y_{TP}}{Y_{CP}Y_{TP}}p_t + \frac{(1 - \mu_{s\ell p})}{S_{LP}}\tau_\ell - 1 \le 0,\end{aligned} \tag{13}$$

where $\mu_{s\ell p}$ and μ_{tp} are the plastic envelope shape coefficients, Y_{CP} and Y_{TP} are the transverse compressive and tensile yield stresses, respectively, and S_{LP} is the longitudinal shear yield stress. The yield stresses are defined as a function of a plastic internal variable called the equivalent plastic strain ($\bar{\varepsilon}^p$). In the present constitutive model, the evolution of the yield stresses is defined using a yield stress vs. $\bar{\varepsilon}^p$ curve for each of them. The evolution of the equivalent plastic strain rate is defined as

$$\dot{\bar{\varepsilon}}^p := \sqrt{\frac{1}{2}}\left\|\dot{\boldsymbol{\varepsilon}}^p\right\|. \tag{14}$$

In addition, the non-associative flow rule presented in [23] is applied,

$$\dot{\boldsymbol{\varepsilon}}^p := \lambda\frac{\partial \varphi^p}{\partial \boldsymbol{\sigma}}, \tag{15}$$

where λ is the plastic multiplier parameter [25] and φ^p is the plastic potential function,

$$\begin{aligned}\varphi^p(\boldsymbol{\sigma}) := &\sqrt{\left(\frac{\hat{Y}_{CP} + \hat{Y}_{TP}}{\hat{Y}_{TP}\hat{Y}_{CP}}\right)^2 \frac{\tau_t^2 + \hat{\mu}_{tp}p_t^2}{1 + \hat{\mu}_{tp}} + \left(\frac{\hat{\mu}_{s\ell p}}{\hat{S}_{LP}}\tau_\ell\right)^2} \\ &+ \frac{\hat{Y}_{CP} - \hat{Y}_{TP}}{\hat{Y}_{TP}\hat{Y}_{CP}}p_t + \frac{(1 - \hat{\mu}_{s\ell p})}{\hat{S}_{LP}}\tau_\ell - 1,\end{aligned} \tag{16}$$

where $\hat{Y}_{CP}$ and $\hat{Y}_{TP}$ are the transverse compressive and tensile plastic potential stresses, respectively, $\hat{S}_{LP}$ is the longitudinal shear plastic potential stress, and $\hat{\mu}_{tp}$ and $\hat{\mu}_{s\ell p}$ are the plastic potential envelope shape coefficients. The parameters of Eq. (16) are defined as constant parameters.

2.2. Damage evolution

Damage activation functions based on effective stresses (or strains) can be expressed as

$$F_N := \phi_N - r_N \le 0, \tag{17}$$

where $\phi_N(\bar{\boldsymbol{\sigma}})$ is a loading function in which $\bar{\boldsymbol{\sigma}}$ only depends on strains and material constants (Eq. (2)) and r_N is an internal damage variable related to a damage mechanism $N = \ell T, \ell C, t$. Expressed in this way, this internal variable can be explicitly integrated as

$$r_N = \max\left(1, \max_{s\in[0,t]}\left(\phi_N^s\right)\right), \tag{18}$$

since ϕ_N only depends on $\boldsymbol{\varepsilon}$.

Three loading functions were considered in Cózar et al. [23]: (i) $\phi_{\ell T}$ for longitudinal tensile loading conditions; (ii) $\phi_{\ell C}$ for longitudinal compressive loading conditions; and (iii) ϕ_t for transverse loading conditions. The loading functions in [23] were defined as

$$\phi_{\ell T} := \frac{\varepsilon_{11}^e E_{11}}{X_T}, \tag{19}$$

where X_T is the longitudinal tensile strength;

$$\phi_{\ell C} := \frac{1}{X_C}\left(\sqrt{\tilde{\sigma}_\ell^2 + \eta_t^q\tilde{p}_t^2 + \eta_{s\ell}^q\tilde{\tau}_\ell^2} + \eta_t\tilde{p}_t + \eta_{s\ell}\tilde{\tau}_\ell\right), \tag{20}$$

where X_C is the longitudinal compressive strength, and $\eta_t, \eta_t^q, \eta_{s\ell}$ and $\eta_{s\ell}^q$ are failure envelope shape coefficients to modify the failure envelope related to the longitudinal compressive loading states, see Fig. 2.a,b; and

$$\phi_t := \sqrt{\left(\frac{Y_C + Y_T}{Y_TY_C}\right)^2 \frac{\tilde{\tau}_t^2 + \mu_t\tilde{p}_t^2}{1 + \mu_t} + \left(\frac{\mu_{s\ell}}{S_L}\tilde{\tau}_\ell\right)^2} + \frac{Y_C - Y_T}{Y_TY_C}\tilde{p}_t + \frac{(1 - \mu_{s\ell})}{S_L}\tilde{\tau}_\ell, \tag{21}$$

where Y_C and Y_T are the transverse compressive and tensile strengths, respectively, S_L is the longitudinal shear strength, and μ_t and $\mu_{s\ell}$ are failure envelope shape coefficients to modify the failure envelope related to the transverse loading states, see Fig. 2.c,d.

The longitudinal damage variable in Eq. (5) is defined as

$$d_\ell := d_{\ell T}\frac{\langle\sigma_\ell\rangle}{|\sigma_\ell|} + d_{\ell C}\frac{\langle -\sigma_\ell\rangle}{|\sigma_\ell|}, \tag{22}$$

where $\langle x\rangle$ is the McCauley operator defined as $\langle x\rangle := (x + |x|)/2$, and $d_{\ell T}$ and $d_{\ell C}$ are the longitudinal tensile and compressive damage variables, respectively. They are defined as a function of the corresponding r_N and using a bilinear softening law [23]. Therefore, different evolution of the longitudinal damage variable is considered (one in tension and another in compression). The damage evolution in mode-I matrix cracking is assumed equal to the one obtained in mode-II matrix cracking when the matrix crack opens. However, the mode-I degradation is not considered when the matrix crack closes [15,23],

$$d_t := d_{st}\frac{\langle p_t\rangle}{|p_t|}. \tag{23}$$

In addition, it is assumed that the stiffness degradation in the longitudinal shear direction is also influenced by the longitudinal tensile stress [6,15,23] as

$$d_{s\ell} := 1 - (1 - d_{s\ell^*})(1 - d_{\ell T}), \tag{24}$$

where $d_{s\ell^*}$ is the damage related to the pure longitudinal shear stresses [15,23].

The previous formulation can produce spurious damage, as explained before. That is clearly presented in Fig. 1 where a large ε_{11}^e generates transverse effective stresses (due to the d_ℓ) and spurious transverse damage. This phenomenon is not account for the longitudinal tensile damage because $\phi_{\ell T}$ in Eq. (19) only depends on ε_{11}^e, since a non-interacting maximum allowable strain criteria is employed. However, while this event can arise at $\phi_{\ell C}$ from Eq. (20) this is suitable since longitudinal compressive failure mechanisms are promoted by matrix cracking in FRP composite materials. Longitudinal compressive failure is promoted by fibre collapse as a result of shear kinking (due to small initial fibre misalignments) and matrix cracking [26,27]. In addition, the transverse failure directly affects the longitudinal compressive stiffness since the matrix is not capable of containing the fibres promoting fibre-microbuckling.

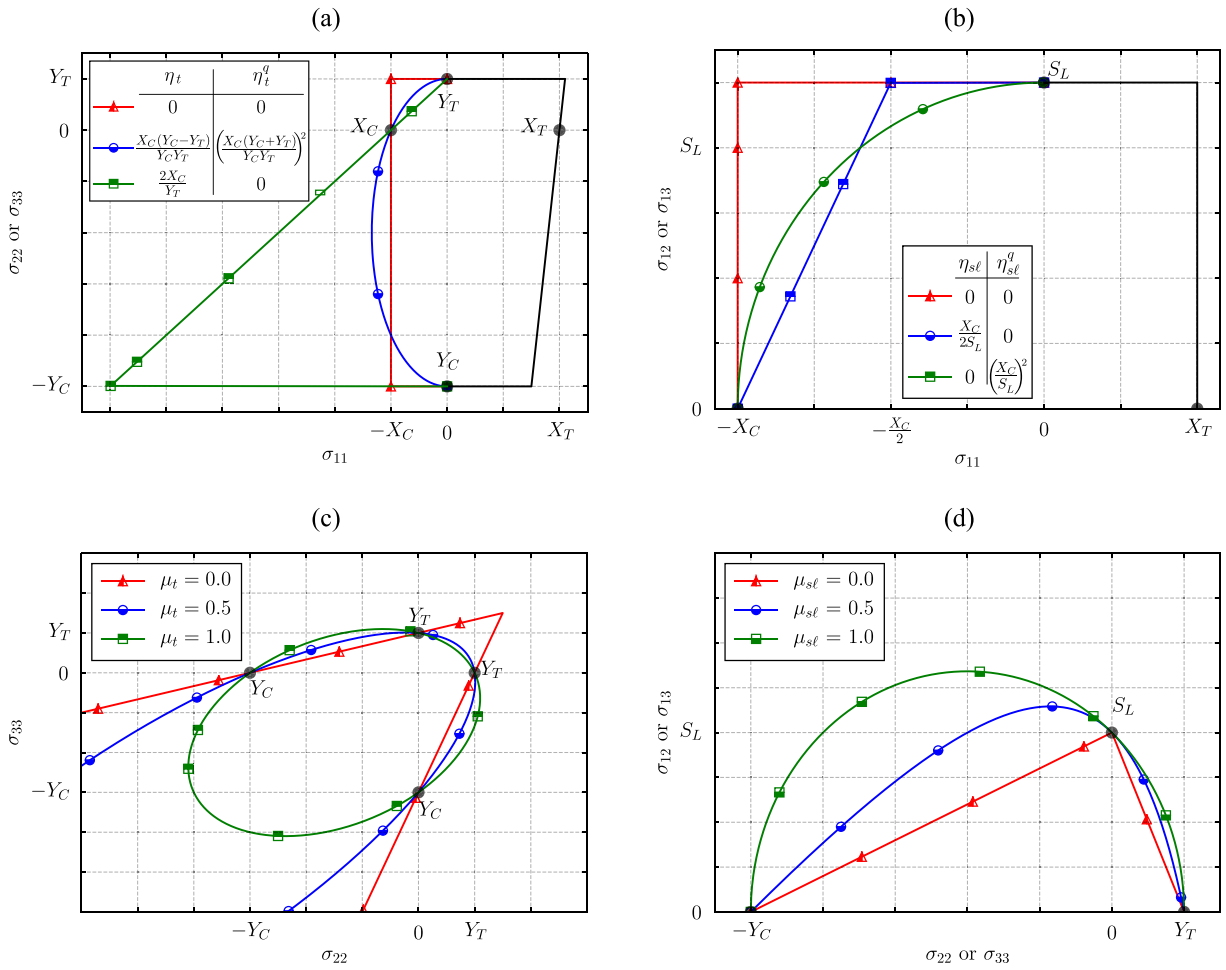

Fig. 2. Schematic representation of the failure envelope for the stress space for $d_M = 0$: (a) $\sigma_{11} - \sigma_{22}$, (b) $\sigma_{11} - \sigma_{12}$, (c) $\sigma_{22} - \sigma_{33}$, and (d) $\sigma_{22} - \sigma_{12}$. Note that, (b) and (d) are symmetric with respect to their X-axis.

In FRP composite materials, the onset of a crack in any direction governed by the matrix is reached with less stress compared to the stress required to initiate a crack in the pure longitudinal direction. Therefore, the longitudinal damage variables do not usually experience the spurious damage phenomenon discussed in the present work. Based on the previous observations, ϕ_t (see Eq. (21)) is modified as a function of the nominal stress tensor instead of the effective stress tensor. Therefore, ϕ_t is not affected by pure longitudinal loading conditions. The transverse activation function is rewritten as

$$F_t := \phi_t - 1 \leq 0, \tag{25}$$

and the transverse loading function as ($\boldsymbol{\sigma}$ instead of $\tilde{\boldsymbol{\sigma}}$ in Eq. (21))

$$\phi_t := \sqrt{\left(\frac{Y_C^d + Y_T^d}{Y_T^d Y_C^d}\right)^2 \frac{\tau_t^2 + \mu_t p_t^2}{1+\mu_t} + \left(\frac{\mu_{s\ell}}{S_L^d}\tau_\ell\right)^2} + \frac{Y_C^d - Y_T^d}{Y_T^d Y_C^d} p_t + \frac{(1-\mu_{s\ell})}{S_L^d}\tau_\ell, \tag{26}$$

where the index $(\cdot)^d$ in strengths refers to them being from the material currently damaged. Therefore, these strengths must be defined as a function of the corresponding damage variable (current strengths) since the loading function is evaluated with the nominal stress tensor. Otherwise, only the onset of damage and not the evolution of the damage would be captured. For example, in a pure transverse tensile test $\sigma_{22} = Y_T$ only in the onset of damage, after that $\sigma_{22} < Y_T$. The current strengths are obtained assuming linear softening laws for the transverse damage variables as in [23] (see Fig. 3) and applying: pure transverse compressive state stress conditions for $Y_C^d(d_{st})$; pure transverse tensile state stress conditions for $Y_T^d(d_{st})$; and pure longitudinal shear state stress conditions for $S_L^d(d_{s\ell^*})$. They read

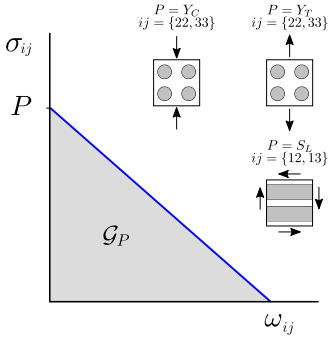

Fig. 3. Stress vs. opening crack (ω_{ij}) curves of the softening laws in the transverse directions.

$$Y_C^d = \frac{4Y_C \mathcal{G}_{Y_C} E_{22}(1-d_{st})}{4\mathcal{G}_{Y_C} E_{22}(1-d_{st}) + l_t^*(\nu_{23}-1)(Y_C d_{st})^2 + 2Y_C^2 l_t^* d_{st}}, \tag{27}$$

$$Y_T^d = \frac{2Y_T \mathcal{G}_{Y_T} E_{22}(1-d_{st})}{2\mathcal{G}_{Y_T} E_{22}(1-d_{st}) + Y_T^2 l_t^* d_{st}}, \tag{28}$$

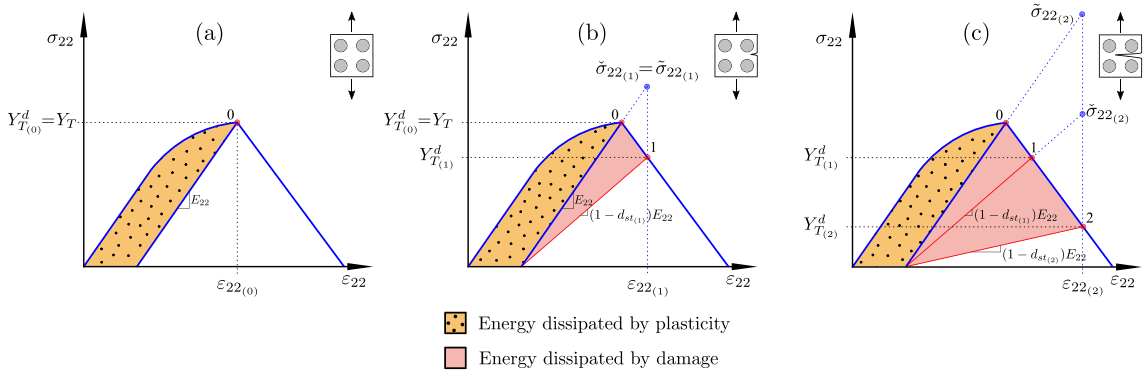

Fig. 4. Schematic representation of the numerical implementation of the damage of the present constitutive model at the Gauss-point level when a pure transverse tensile test is applied: (a) undamaged stress state; (b) onset of a matrix crack; and (c) propagation of a matrix crack.

and

$$S_L^d = \frac{2\mathcal{G}_{S_L} S_L G_{12}(1-d_{s\ell^*})}{2\mathcal{G}_{S_L} G_{12}(1-d_{s\ell^*}) + S_L^2 l^*_{s_\ell} d_{s\ell^*}}, \tag{29}$$

where $\mathcal{G}_P$ $(P = Y_C, Y_T, S_L)$ is the fracture toughness of the corresponding direction, and l_t^* and $l^*_{s_\ell}$ are the characteristic element length at the transverse and longitudinal shear directions, respectively. The calibration of the envelope shape coefficients of Eqs. (20) and (26) is explained in detail in [23].

3. Constitutive model implementation

The implementation of the present constitutive model for an explicit FE solver at the Gauss-point level is explained below. The damage variable corresponding to the longitudinal direction (d_ℓ) is explicitly obtained as in the original model [15,23], since the same damage activation functions (Eq. (17)) are used. However, the damage variables corresponding to the transverse direction (d_{st} and $d_{s\ell^*}$) must be obtained from the transverse damage activation function in Eq. (25).

FE models with explicit solvers use very small increments of the strain tensor, especially for FRP composite materials. Therefore, the variation of the stress tensor and of the internal variables is very small between each increment of the strain tensor. The implementation algorithm presented here is based on the fact that the solution at time $t_{(n+1)}$ is close to solution at the converged solution at the previous time interval ($t_{(n)}$).

The schematic representation of the modelled damage for a pure transverse tensile test at the Gauss-point level is presented in Fig. 4; note that the displayed strain increment is high for the sake of the algorithm explanation. Firstly, the elastic–plastic behaviour is considered without damage (see Fig. 4.a). Then, the matrix crack onset is observed and, therefore, no further development of plasticity will evolve [23]. From point 0 to 1 in Fig. 4.b, a predictor stress tensor ($\check{\boldsymbol{\sigma}}$) is calculated using $\mathbb{C}_e$ as a function of the damage variables of the previous time interval ($d_{M_{(n)}}$) as

$$\check{\boldsymbol{\sigma}}_{(n+1)} := \mathbb{C}_e(d_{M_{(n)}})\boldsymbol{\varepsilon}^e_{(n+1)}. \tag{30}$$

Therefore, the predicted and effective stress tensors are the same when the material is undamaged ($d_{M_{(n)}} = 0 \rightarrow \check{\boldsymbol{\sigma}} = \tilde{\boldsymbol{\sigma}}$). However, if the Gauss-point is damaged at the previous time interval, the predicted and effective stress tensors are not the same ($d_{M_{(n)}} > 0 \rightarrow \check{\boldsymbol{\sigma}} \neq \tilde{\boldsymbol{\sigma}}$), see Fig. 4.c from points 1 to 2. After that, $\phi_{t_{(n+1)}}$ is evaluated as a function of $\check{\boldsymbol{\sigma}}(d_{M_{(n)}})$ and the current transverse strengths from Eqs. (27)–(29) with $d_{M_{(n)}}\left(Y_C^d(d_{st_{(n)}}), Y_T^d(d_{st_{(n)}})\right.$ and $\left.S_L^d(d_{s\ell^*{}_{(n)}})\right)$.

A new internal transverse damage variable (r_t) is introduced to account for the history of the transverse damage, then d_{st} and $d_{s\ell^*}$ are obtained as a function of r_t. When the transverse damage evolves, the imposed condition by Eq. (25) is achieved by linearising F_t as

$$F_{t_{(n+1)}} + \frac{\partial F_{t_{(n+1)}}}{\partial r_{t_{(n+1)}}} \Delta r_{t_{(n+1)}} = 0. \tag{31}$$

Considering that Eq. (26) satisfies

$$\frac{\partial F_{t_{(n+1)}}}{\partial r_{t_{(n+1)}}} \approx -\frac{1}{r_{t_{(n)}}}, \tag{32}$$

and introducing Eq. (32) in Eq. (31), the internal transverse damage variable at the current time yields

$$r_{t_{(n+1)}} = \phi_{t_{(n+1)}} r_{t_{(n)}}. \tag{33}$$

Finally, to guarantee that r_t monotonically increases, then

$$r_{t_{(n+1)}} = \max\left(r_{t_{(n)}}, \phi_{t_{(n+1)}} r_{t_{(n)}}\right), \tag{34}$$

where the initial r_t must be defined equal to 1. The residue from the first iteration is negligible when FE explicit solver is employed.

In summary, the implementation is based on the approach applied in the constitutive models with $\tilde{\boldsymbol{\sigma}}$. The main difference is that F_t is evaluated with the damaged material properties and the applied stress tensor. The graphical comparison of the proposed implementation method with the one used in constitutive models with $\tilde{\boldsymbol{\sigma}}$ under a pure transverse tensile loading state is presented in Fig. 5. The current predictor stress tensor ($\check{\boldsymbol{\sigma}}_{(n+1)}$) is equal to the effective stress tensor calculated by degrading the corresponding stiffness using $d_{M_{(n)}}$ ($\tilde{\boldsymbol{\sigma}}_{(n+1)}(\mathbb{C}_e(d_{M_{(n)}}))$). Similar behaviour is obtained when the transverse internal damage variable r_t is compared. Therefore, the evolution of the transverse damage variables as a function of r_t yields the one in constitutive models with $\tilde{\boldsymbol{\sigma}}$. The transverse damage is guaranteed to increase since $r_{t_{(n+1)}}$ in Eq. (34) always increases and the transverse damage variables as a function of $r_{t_{(n+1)}}$ are monotonically increasing functions.

The longitudinal elastic domain thresholds ($\phi_{\ell T}, \phi_{\ell C}$) are explicitly obtained from Eq. (18). All damage variables (longitudinal and transversal) are obtained from the expressions presented in [15,23] using the strengths from the undamaged material. The return mapping for the plastic modelling and its coupling with the damage modelling presented in [23] is employed in the present work. Algorithm 1 in Appendix summarises the workflow to implement the constitutive model at the Gauss-point level using an explicit solver in a nonlinear FE framework.

4. Numerical predictions

The improvement of the present formulation is demonstrated by comparing the results using the present constitutive model with those

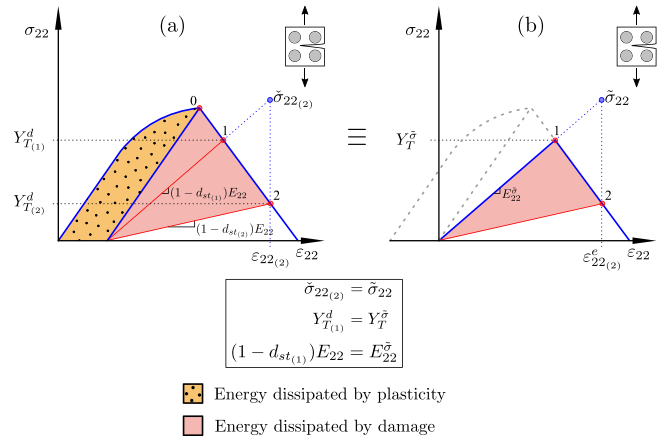

Fig. 5. Schematic representation of the numerical implementation of the damage of the present constitutive model at the Gauss-point level when a pure transverse tensile test is applied: (a) proposed implementation; (b) equivalent implementation using the effective stress tensor and damaged material properties.

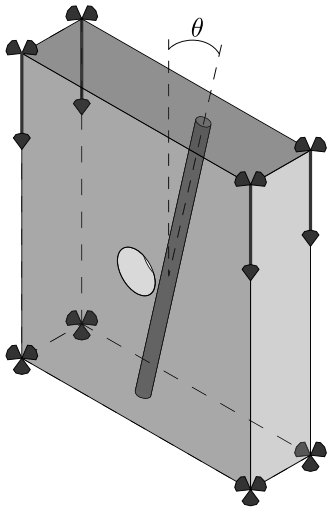

Fig. 6. Schematic representation of the boundary conditions applied in the open-hole compressive simulations. θ is the fibre angle orientation.

obtained from the previous model developed by Cózar et al. [23], which is a CDM model based on $\tilde{\boldsymbol{\sigma}}$. A longitudinal virtual tensile test at Gauss-point level is performed in Section 4.1. The stresses and damage variables vs. strain curves of the longitudinal and transverse direction are presented. Next, an OHC test using a quasi-isotropic laminate is carried out in Section 4.2. The comparison of the numerical results from both models with the experimental data is used to analyse the impact of the new model on the predictions. After that, an OHC test using a unidirectional stacking sequence at 0° is presented in Section 4.3 since the failure strength of OHC tests in quasi-isotopic laminates is governed by the plies at 0°. This comparison can help to explain the possible discrepancies on the predicted failure strength obtained from each model in the quasi-isotropic laminate. Finally, an OHC test using a unidirectional stacking sequence at 90° is performed in Section 4.4. This last comparison can help to explain the possible discrepancies on the predicted failure pattern in the quasi-isotropic laminate.

The present constitutive model is implemented in a user material subroutine VUMAT and is linked with the Abaqus/Explicit solver [28]. The mesh element size selected is less than four times the critical element size (0.1 mm) to prevent snap-back of the constitutive softening laws for each failure mode [29] around the regions where damage is

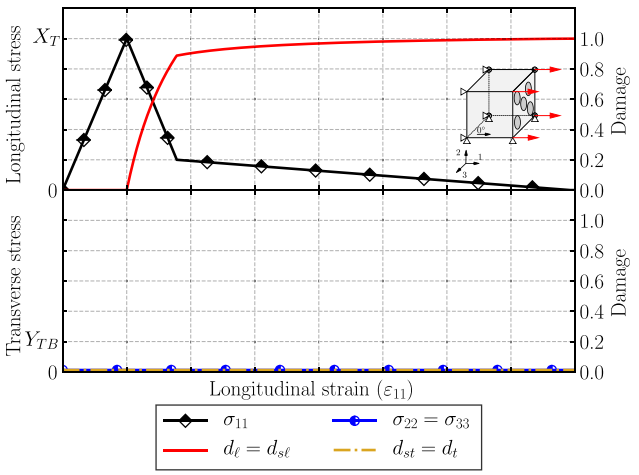

Fig. 7. Longitudinal virtual tensile test at the Gauss-point level using the present constitutive model, where Y_{TB} is the biaxial transverse tensile strength. (Top) Longitudinal response, and (bottom) transverse response.

expected in the open-hole tests. In addition, three elements through-the-thickness of each ply are used. For all the simulations presented, 3D eight-node C3D8R solid elements with reduced integration are used. The C3D8R solid elements are widely used in FE simulations with constitutive models based on the crack band model, such as open-hole and filled-hole test [30], low velocity impact and compression after impact test [31], single-bolt joints [32,33], composite pressure vessels [34], etc. Reduced integration elements are used to alleviating the overstiffness of the elements away from the hole due to their high aspect ratio [35]. Reduced integration elements also allow to reduce the computational time compare to the full integration elements. Furthermore, the use of three elements through-the-thickness per ply mitigate the hourglass effect.

A carbon FRP composite material is employed in the simulations, IM7/8552 unidirectional prepreg system with a nominal thickness of 0.131 mm [36]. The material properties required by the model are listed in Table 1. The envelope shape coefficients are those reported in [15]. They were obtained fitting the failure criteria previously developed by Camanho et al. [19], which were developed by combining experimental data and micromechanical models for the selected material in this work. In addition, the yielding stresses vs. $\bar{\varepsilon}^p$ required to model the plastic strains are obtained from [37]. The fracture toughness in the transverse compressive direction ($\mathcal{G}_{Y_C}$) is adjusted to fit the experimental data of a single OHC test presented in [38]. In this case, the hole diameter of the specimen selected to adjust the parameter is equal to 3 mm. The numerical modelling strategy used to adjust $\mathcal{G}_{Y_C}$ follows the one presented in [23]. The relative error between the numerical and mean experimental values of the failure strength is equal to 0.18%.

The boundary conditions presented in Fig. 6 are applied in the open-hole virtual tests. The displacement on the upper face of the specimens is applied at low velocity to avoid dynamic effects, while the remaining degrees of freedom of this face are constrained. Furthermore, all degrees of freedom on the bottom face of the specimens are constrained. In addition, the out-of-plane displacement on the front and back faces are fixed in the virtual test of Section 4.3 in accordance with Seon et al. [39], who used a support to prevent buckling during experimental tests.

4.1. Longitudinal tensile test

A pure longitudinal virtual tensile test is carried out using the present constitutive model at the Gauss-point level. The longitudinal stress vs. strain curve follows the imposed softening law in the tensile

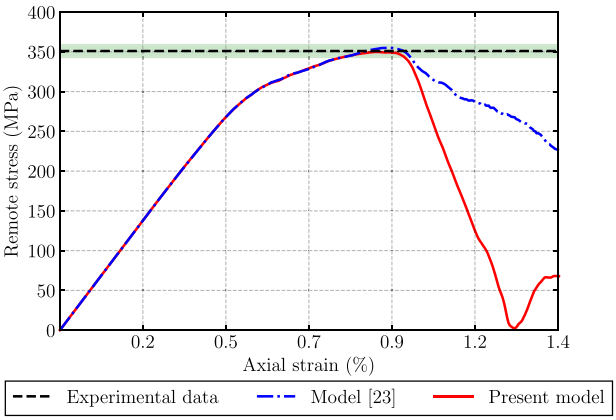

Fig. 8. Numerical-experimental comparison of the remote stress vs. axial strain curves of the open-hole compressive test performed by Wisnom et al. [40]. The green area represents the experimental error of the failure strength assuming a level of confidence equal to 95%.

direction (bilinear softening curve) and the evolution of $d_{s\ell}$ is equal to $d_{\ell T}$ due to the definition of Eq. (24) since $d_{s\ell *}(\phi_t = 0) = 0$, see Fig. 7.a. However, the transverse damage variables are equal to zero ($d_t = d_{st} = d_{s\ell *} = 0$) since the stresses in the transverse directions are equal to zero and, therefore, $\phi_t = 0$, see Fig. 7.b.

The comparison of Fig. 1 with Fig. 7 demonstrates that the CDM which use $\tilde{\sigma}$ can generate spurious damage in the transverse direction when a pure tensile loading condition is applied. However, the presented model in this work avoids transverse damage variables being activated when the Gauss-point is not loaded in the transverse direction ($p_t = \tau_\ell = \tau_t = 0$).

4.2. Open-hole compressive test

The OHC test in a quasi-isotropic laminate $[45/90/-45/0]_{4s}$ and a diameter of 6.35 mm carried out by Wisnom et al. [40] is used in this section. The stress vs. strain curve obtained from the present model matches the one obtained by the model [23] until the onset of damage, see Fig. 8. After that, the evolution of the curves are significantly different. It would be expected that the model [23] which use $\tilde{\sigma}$ suddenly drops when the failure strength is reached since the longitudinal damage generates spurious transverse damage. However, the stress vs. strain curve gradually decreases after the failure strength from the model [23]. This behaviour is explained in Fig. 10.c, the failure is developed in a larger area in comparison of the present model because the spurious damage is extended in the whole specimen. Therefore, the model with $\tilde{\sigma}$ dissipated more energy due to damage than the present model.

Table 1
Model input parameters for the IM7/8552 unidirectional prepreg system.

	Symbol	Value	Unit	Source
Elastic	E_{11}	171 420.00	MPa	[36]
	E_{22}	9 080.00	MPa	[36]
	G_{12}	5 290.00	MPa	[36]
	ν_{12}	0.32	–	[36]
	ν_{23}	0.45	–	[23]
Plastic	$Y_{CP}(\bar{\varepsilon}^p)$	Curve		[37]
	$Y_{TP}(\bar{\varepsilon}^p)$	Curve		[37]
	$S_{LP}(\bar{\varepsilon}^p)$	Curve		[37]
	μ_{tp}	0.47	–	[23]
	$\mu_{s\ell p}$	1.00	–	[23]
	ν^p_{23T}	1.00	–	[37]
	ν^p_{23C}	1.00	–	[37]
	ν^p_{122}	0.00	–	[37]
Damage	X_C	1 017.50	MPa	[41]
	$f_{X_C} X_C$	203.50	MPa	[15]
	$\mathcal{G}_{X_C}$	106.30	N/mm	[36]
	$f_{\mathcal{G}_{X_C}} \mathcal{G}_{X_C}$	26.58	N/mm	[15]
	X_T	2 323.50	MPa	[41]
	$f_{X_T} X_T$	464.70	MPa	[15]
	$\mathcal{G}_{X_T}$	97.80	N/mm	[42]
	$f_{\mathcal{G}_{X_T}} \mathcal{G}_{X_T}$	48.90	N/mm	[15]
	Y_C	253.70	MPa	[15]
	$\mathcal{G}_{Y_C}$	2.8	N/mm	Adjusted in Section 4
	Y_T	62.30	MPa	[36]
	$\mathcal{G}_{Y_T}$	0.28	N/mm	[36]
	S_L	92.30	MPa	[36]
	$\mathcal{G}_{S_L}$	0.80	N/mm	[36]
	μ_t	0.90	–	[15]
	$\mu_{s\ell}$	1.00	–	[15]
	$\eta_{s\ell}$	9.50	–	[15]
	$\eta^q_{s\ell}$	0.00	–	[15]
	η_t	12.00	–	[15]
	η^q_t	350.00	–	[15]

The stress obtained from the present model suddenly drops after the failure strength since the damage is localised at the midplane of the specimen (see Fig. 10.b). In addition, the comparison of predicted failure strength using the present model and the model [23] with the mean value from the experimental tests are in very good agreement. The relative error between the failure strength from the present model and the mean experimental data is equal to 0.32%, and 1.15% from [23]. The green area in Fig. 8 represents the experimental error of the failure strength assuming a level of confidence equal to 95%. Therefore, the predicted failure strength from both models are within the expected dispersion of the experimental data.

Fig. 9 compares the predicted external failure pattern with the experimental data at 98% of the failure load. Only the comparison of $d_{s\ell}$ with the experimental data is presented since the external failure patterns of d_{st} is approximately equal to $d_{s\ell}$ and no fully-

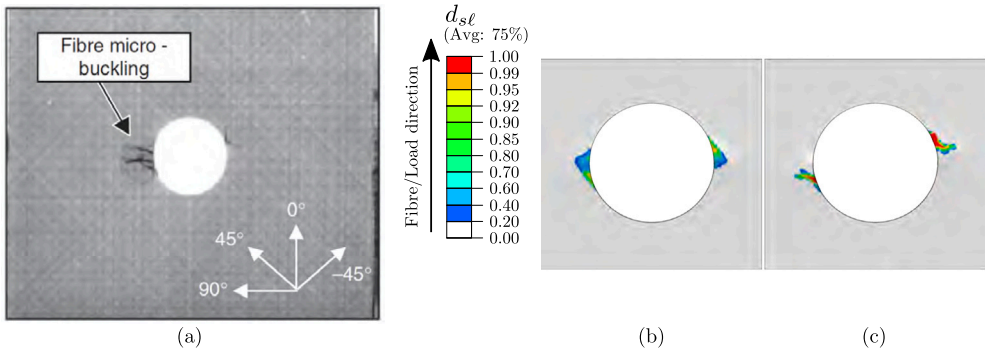

Fig. 9. Numerical-experimental comparison of the failure onset at 98% of the failure remote load from the quasi-isotropic laminate in the open-hole compressive test: (a) experimental data from [40]; (b) present model; and (c) model from [23].

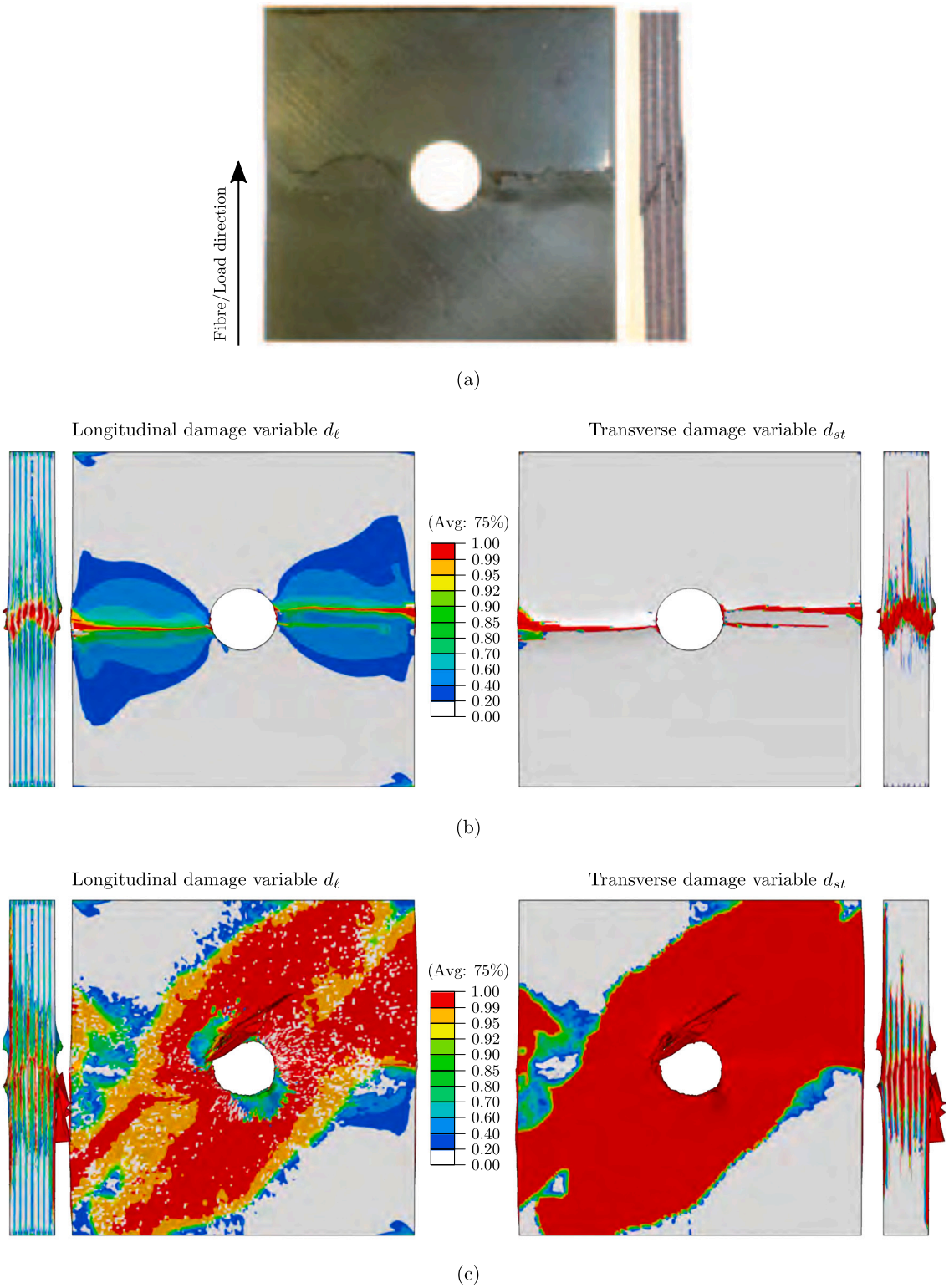

Fig. 10. Numerical-experimental comparison of the external failure pattern after the failure remote load from the quasi-isotropic laminate in the open-hole compressive test: (a) experimental data from Wisnom et al. [40]; (b) present model; and (c) model from [23].

damaged elements are found in d_ℓ and d_t. The initiation of the failure patterns from both constitutive models are in good agreement with the experimental data. In all cases, failure starts in two separate zones around the hole edge with similar in-plane angles.

The predicted failure external patterns after the peak load are compared to the experimental data in Fig. 10. Only the transverse damage variable d_{st} is presented since the failure pattern of $d_{s\ell}$ is approximately equal to d_{st} and negligible failure is found in d_t. The brittle failure mechanism observed in the experimental data is properly captured by the proposed constitutive model. The predicted failure pattern is in good agreement with the fracture straight across the laminate and the out-of-plane fracture plane observed in the experimental data, see Fig. 10.a and b. However, the failure pattern predicted by the constitutive model [23] is not in agreement with the experimental data,

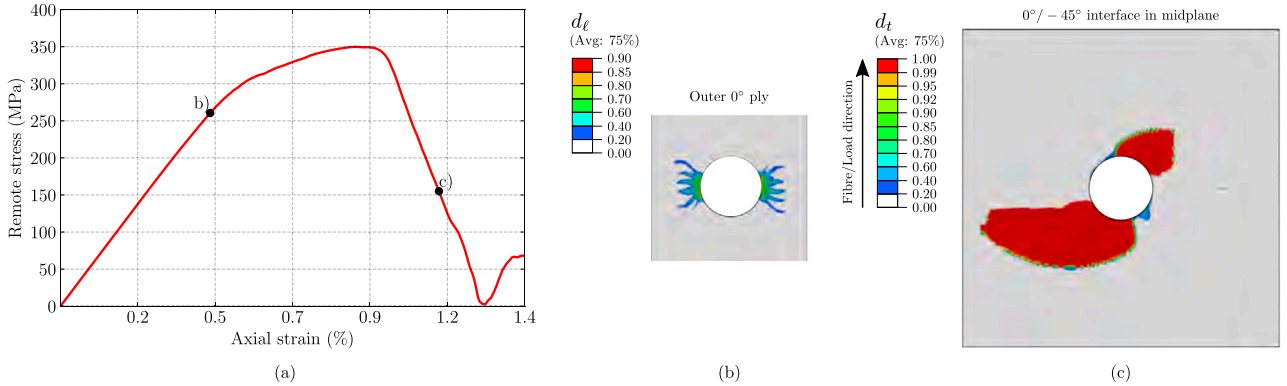

Fig. 11. Predicted failure mechanism evolution of the quasi-isotropic laminate in an open-hole compressive test using the present model: (a) predicted stress vs. strain curve; (b) longitudinal failure pattern of 0° outer ply at 75% of the failure strength; and (c) failure pattern of 0°/−45° interface in the midplane of the specimen after the failure strength.

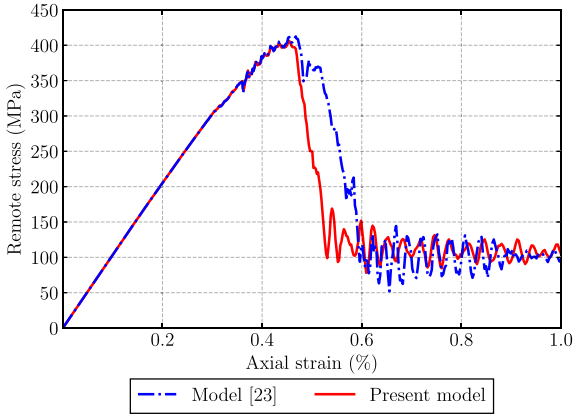

Fig. 12. Predicted remote stress vs. axial strain curves from the open-hole compressive test with $[0]_8$.

see Fig. 10.a and c. Similar behaviour is observed at the peak remote load, the damage is localised around the hole in a fracture straight across the laminate in the present model. However, the failure pattern suddenly grows from the hole to either direction in results from [23].

The localisation of the damage in OHC specimens with multidirectional laminates always initiates at the edges of the hole in the outer 0° plies at about 75÷85% of the failure strength [43–48]. This phenomenon is predicted by the present model, most of the dissipated energy from the longitudinal failure mechanism at 75% of the failure strength is observed at the outer 0° plies, see Fig. 11.b. A negligible failure is found in the rest of the layers at 75% of the failure remote load.

The main failure mechanism in OHC specimens is the fibre microbuckling in the 0° plies, which promotes delamination between the off-axis and 0° plies at the edges of the hole [43–48]. Despite not having specific elements to model delamination as cohesive elements on the ply interfaces, the elements located on the 0° midplane layer in contact with those from the −45° layer show the typical delaminated failure pattern. There are three elements through-the-thickness of each ply and d_t refers to the mode-I matrix cracking. After that, the delamination grows in that interface, see Fig. 11.c

The discrepancies on the failure pattern predicted by [23] with the pattern experimentally obtained does not have significant influence on the failure strength in OHC quasi-isotropic laminates. However, these discrepancies can take an important influence in damage-tolerance design. In the aeronautical and aerospace industry, a composite structure is designed to able to sustain loads even with damage [49]. For example, in compression after impact (CAI) test, firstly the specimen is impacted and, therefore, different damage mechanisms are produced: matrix cracking, fibres fractures and delamination [29]. After that, the specimen is loaded in compression until failure. In the CAI test, the residual strength depends on the local buckling and the propagation of the impacted-induced failure mechanisms previously described [50]. Hence, a good prediction of the failure pattern in the impact test is required to properly predict the CAI strength. The CAI strength decrease when the delaminated area increases [29,51,52]. Therefore, if the delaminated area is not properly predicted, the constitutive model cannot capture the CAI strength.

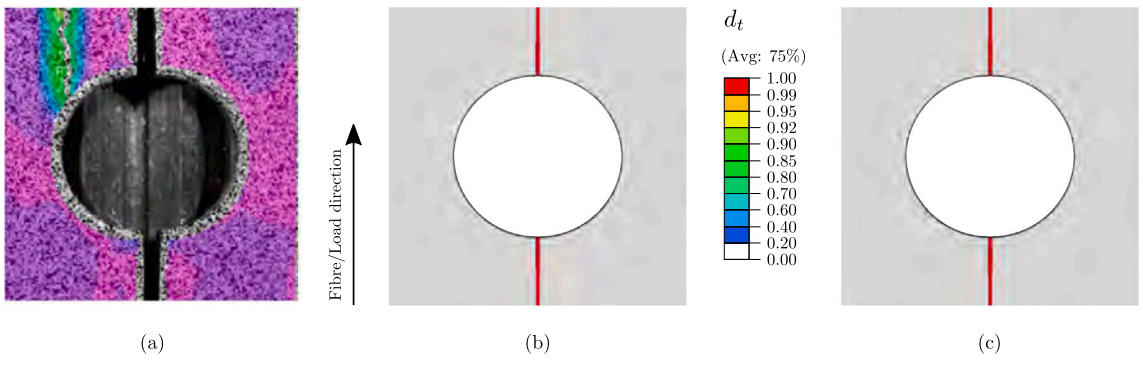

Fig. 13. Numerical-experimental comparison of the failure pattern at the failure remote load from the $[0]_8$ laminate in the open-hole compressive test: (a) experimental data from Seon et al. [39]; (b) present model; and (c) model from [23].

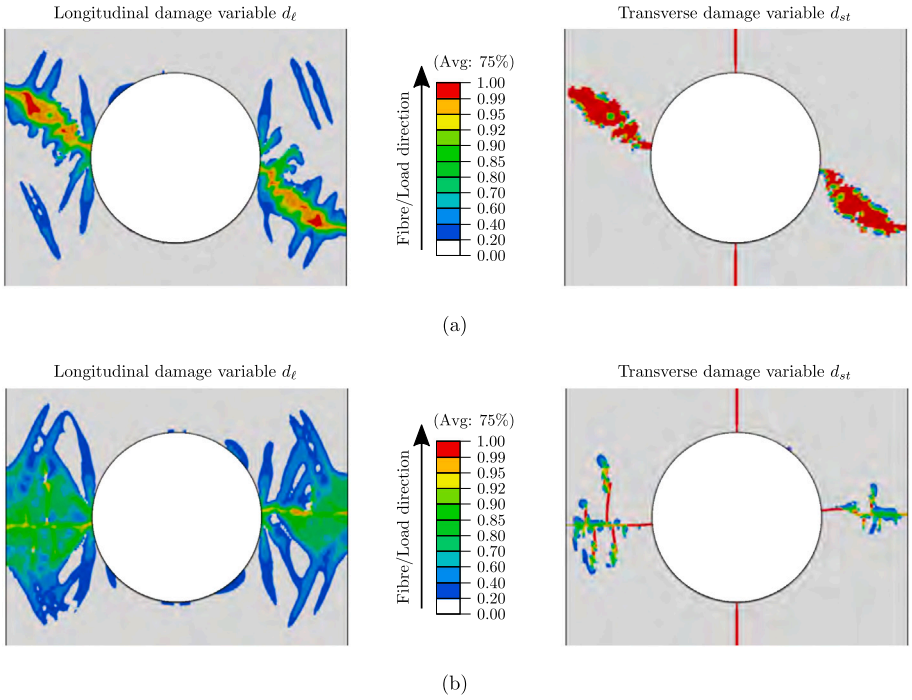

Fig. 14. Predicted external failure patterns after the failure remote load of the $[0]_8$ laminate in an open-hole compressive test using: (a) present model; and (b) model from [23].

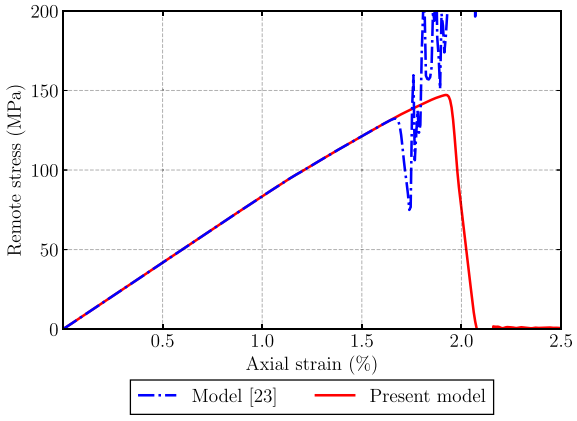

Fig. 15. Predicted remote stress vs. axial strain curves from the open-hole compressive test with $[90]_8$.

4.3. Open-hole compressive test at 0°

As previously mentioned, the failure strength in OHC tests of multidirectional laminates is governed by the 0° layers [43–48]. For this reason, an OHC virtual test with all plies aligned with respect to the load direction is used to explain the agreement of the predicted failure strength from the present model and [23] in Fig. 8. In addition, the OHC test carried out by Seon et al. [39] is employed to compare the predicted onset failure pattern. The hole diameter of the specimen used in the virtual tests is equal to 6.35 mm and the in-plane dimensions are 12.8 mm × 25.6 mm as defined in [39], and eight plies at 0° with respect to the loading direction are used (as in Section 4.2).

The comparison of the stress vs. strain curve obtained from the present model and [23] is performed in Fig. 12. Good agreement between both predicted curves is found until the failure strength. After that, the curves differently drop and, finally, the stress stabilises around 100 MPa in both cases. This observation could explain the agreement in the predicted failure strength from OHC specimens with quasi-isotropic laminates. The failure strength in quasi-isotropic laminates is governed by 0° layers and no significant discrepancies in the failure strength from the 0° unidirectional laminates are obtained.

Fig. 13 compares the external predicted failure pattern at the failure strength with the experimental data reported by Seon et al. [39]. A matrix crack is observed in all cases (the experimental data and the numerical predictions). Good agreement is found on the failure mechanism between the predictions and the experimental data. In contrast, the predicted failure patterns obtained after the failure load from both models are significantly different, see Fig. 14. The cracks predicted after the failure load by the present model grow with an inclination from the hole edge to the lateral edges (Fig. 14a), whereas the cracks predicted by the model [23] grow horizontally, see Fig. 14.b. That can explain the discrepancies obtained in the failure pattern of the quasi-isotropic laminate in Fig. 10.

4.4. Open-hole compressive test at 90°

OHC virtual tests at 90° are carried out to better understand the discrepancies obtained in the predicted failure pattern from the quasi-isotropic laminate in Section 4.2. The dimensions of the specimen are 31.75 mm × 31.75 mm, the hole diameter is defined equal to 6.35 mm and eight plies at 90° with respect to the load direction.

The stress vs. strain curve predicted from the present model match the one obtained from the model [23] until the failure strength of the latter model is reached, see Fig. 15. After that, the results from [23] are unstable and very large values of the remote load are obtained.

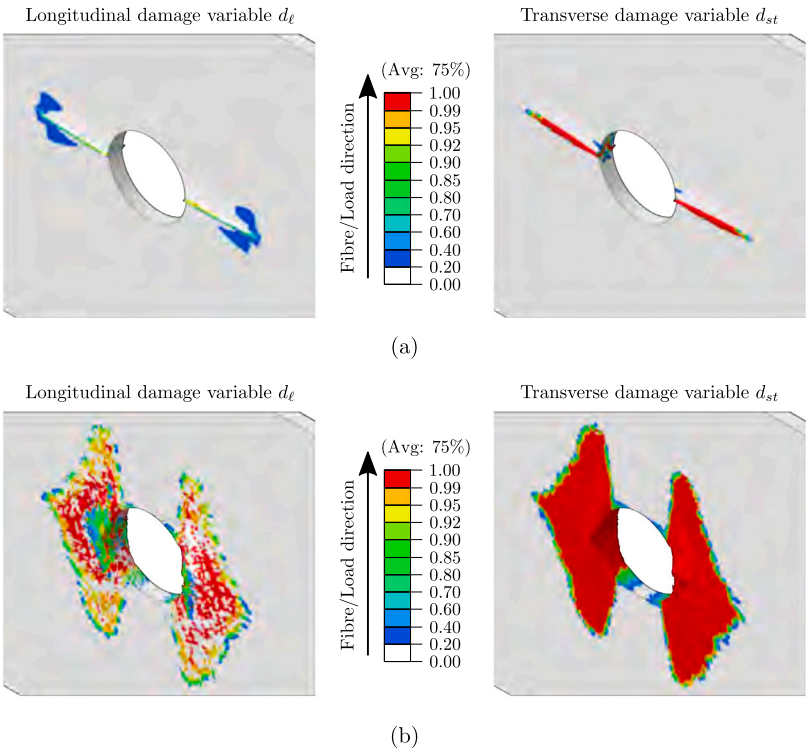

Fig. 16. Predicted failure mechanism at the failure strength of the $[90]_8$ laminate in an open-hole compressive test using: (a) present model; and (b) model from [23].

However, the stress vs. strain curve predicted by the present model increases until the failure strength and, after that, suddenly decreases until 0 MPa. The percent difference between the predicted failure strength obtained by each model is 10.65%. This difference does not have a significant impact on the predicted stress vs. strain curve until the failure strength of an OHC virtual test with a multidirectional laminate, since they are dominated by the 0° layers.

The external failure patterns predicted by model [23] at the failure strength is significantly different from those obtained with the present model, see Fig. 16. In the present model, two matrix cracks are localised at the midplane of the specimen at the hole edge and they are horizontally propagated to the specimen edge, see Fig. 16.a. However, the model [23] not only predicts two matrix cracks at the hole edge growing in the horizontal direction, but also in the vertical direction, see Fig. 16.b. In addition, the fibre failure predicted by the present model is negligible, but fully-damaged elements are found in the predictions of [23].

The constitutive models which use $\tilde{\boldsymbol{\sigma}}$ can generated spurious damage due to damage in the other directions. After the onset of damage in one direction, the effective stresses in other directions increase. Therefore, the activation of the damage functions in the rest of the directions can be achieved. Longitudinal failure promotes artificial transverse cracking, which in turn, also promotes artificial longitudinal failure. That becomes in an unstable damage evolution accentuated after the failure strength. This could explain the fibre damage field in Fig. 16.b. The present constitutive model does not experience that phenomenon because the evolution the transverse variables is not affected by d_ℓ. Therefore, no spurious transverse damage can affect to d_ℓ.

Fig. 17 displays the failure pattern and the deformed shape of the numerical results when 2.25% of the axial strain is applied. The failure pattern and the deformed shape of the specimen from the present model are in agreement with the expected results. Matrix cracks are localised at the hole edge and propagated to the specimen edge, as well as, the out-of-plane displacement of the layers at the midplane. Hence, the matrix cannot contain the fibres and, therefore, the longitudinal compressive damage is activated at the midplane of the specimen. However, all elements are fully-damaged in the transverse direction from [23], therefore, the elements present a large distortion, see Fig. 17.b. The large distorted elements in Fig. 17.b are removed, otherwise, the results cannot be analysed.

5. Conclusions

A methodology to prevent spurious damage generated on the constitutive models which use the effective stress tensor is presented. The proposed approach can be straightforwardly implemented in previously developed constitutive models. In addition, an explicit implementation of the constitutive model linked with a finite element explicit solver is presented. The numerical results obtained from the present constitutive model and those obtained from a model which use the effective stress tensor are compared with experimental data obtained from an open-hole compressive test using a quasi-isotropic laminate. The comparison demonstrates the improvements that the present model brings to predicted failure mechanisms. Good agreement on the failure patterns between the proposed model and the experimental data, as well as on the failure strength, are found. However, the model which use the effective stress tensor does not capture the failure pattern after the failure strength. In addition, two unidirectional virtual test are carried out to explain the improvements seen on the quasi-isotropic laminate. Discrepancies on the failure strength on 90° laminate is found between the models. The present constitutive model predicts the expected deformed shape and failure propagation. However, the model which use the effective stress tensor becomes unstable in terms of failure propagation after the failure remote load, and its deformed shape is inconsistent with the expected shape.

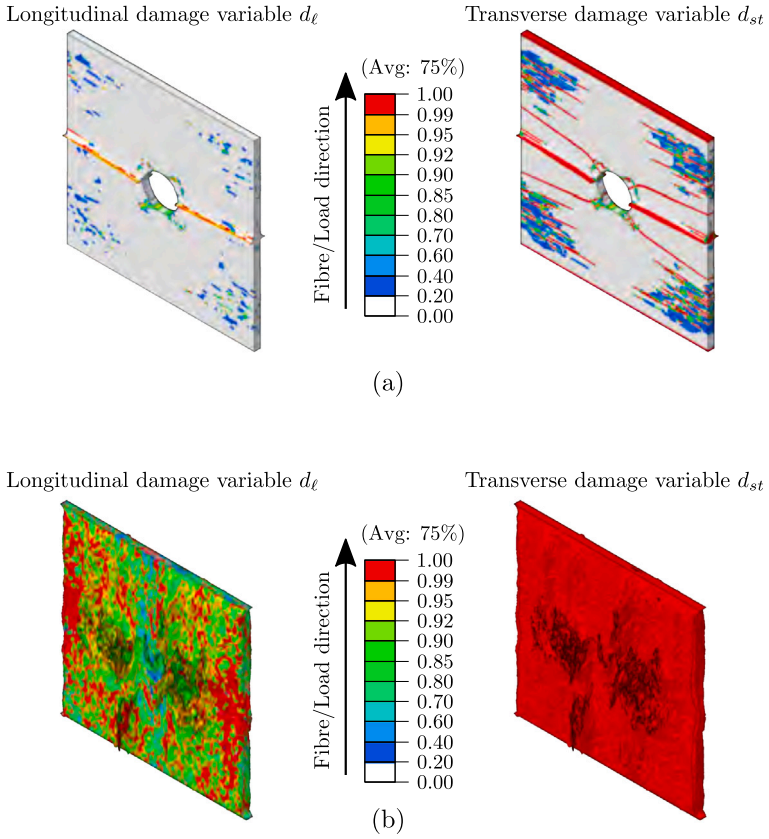

Fig. 17. Predicted failure pattern when 2.25% of the axial strain is applied from the $[90]_8$ laminate in the open-hole compressive test: (a) present model; and (b) model from [23]. The large distorted elements in (b) are removed.

The work presented in this paper solves the long-standing problem of the onset and propagation of spurious damage mechanics related to the use of effective stress tensors in the formulation of continuum damage models. This phenomenon, absent in the model presented here, can have detrimental effects in the simulation of the ultimate failure of composite laminates.

CRediT authorship contribution statement

I.R. Cózar: Conceptualization, Methodology, Software, Validation, Formal analysis, Investigation, Data curation, Writing – original draft. **F. Otero:** Conceptualization, Methodology, Software, Validation, Formal analysis, Supervision, Project administration, Investigation, Writing – review & editing. **P. Maimí:** Conceptualization, Methodology, Validation, Formal analysis, Supervision, Project administration, Writing – review & editing. **E.V. González:** Conceptualization, Methodology, Validation, Formal analysis, Supervision, Project administration, Writing – review & editing. **A. Turon:** Project administration, Funding acquisition. **P.P. Camanho:** Project administration, Funding acquisition.

Declaration of competing interest

The authors declare the following financial interests/personal relationships which may be considered as potential competing interests: Albert Turon and Emilio Gonzalez reports financial support was provided by European Commission. Pere Maimi reports financial support was provided by Spain Ministry of Science and Innovation. Ivan Cozar reports financial support was provided by Agència de gestió d'ajuts universitaris i de recerca, govern de Catalunya.

Data availability

The authors do not have permission to share data.

Acknowledgements

The first author would like to acknowledge the support of the Catalan Government (Agència de Gestió d'Ajuts Universitaris i de Recerca), Spain through Grant 2019FI_B_01117. This work has received funding from the Clean Sky 2 Joint Undertaking (JU), Spain under grant agreement No. 864723. The JU receives support from the European Union's Horizon 2020 research and innovation programme and the Clean Sky 2 JU members, Spain other than the Union. This work also has been partially funded by the Spanish Government (Ministerio de Ciencia e Innovación) under contracts PID2021-126989OB-I00. Open Access funding provided thanks to the CRUE-CSIC, Spain agreement with Elsevier.

Appendix. Algorithm for explicit finite element solver

This appendix presents the algorithm of the present constitutive model used within an explicit solver at Gauss-point level in 1.

Algorithm 1: Algorithm of the present constitutive model at time $t_{(n+1)}$

Input:
Total strain tensor at $t_{(n+1)}$: $\boldsymbol{\varepsilon}_{(n+1)}$
Internal variables at $t_{(n+1)}$: $\boldsymbol{\varepsilon}^p_{(n)}, \bar{\varepsilon}^p_{(n)}, r_{\ell T_{(n)}}, r_{\ell C_{(n)}}, r_{t_{(n)}}$
Initialisation:
Local Newton–Raphson iteration: $k = 0$
Effective stress tensor: $\tilde{\boldsymbol{\sigma}} = \mathbb{C}_e(d_M = 0)(\boldsymbol{\varepsilon}_{(n+1)} - \boldsymbol{\varepsilon}^p_{(n)})$
Effective stress invariants using $\tilde{\sigma}$ in Eqs. (8)–(11)
Stress tensor of the damage predictor:
$\check{\boldsymbol{\sigma}} = \mathbb{C}_e(d_{M_{(n)}})(\boldsymbol{\varepsilon}_{(n+1)} - \boldsymbol{\varepsilon}^p_{(n)})$
Stress invariants of the damage predictor using $\check{\sigma}$ in Eqs. (8)–(11)
Update the transverse strengths as a function of $d_{M_{(n)}}$ in Eqs. (27)–(29)
Loading functions Eqs. (19), (20) and (26):
$\phi_{\ell T}(\tilde{\boldsymbol{\sigma}}), \phi_{\ell C}(\tilde{\boldsymbol{\sigma}}), \phi_t(\check{\boldsymbol{\sigma}})$
Internal damage variables Eqs. (18) and (34)
Damage variables from [23]: $d_{M_{(n+1)}}$
Elastic predictor: $\boldsymbol{\sigma}^{tr}_{(n+1)} = \mathbb{C}_e(d_{M_{(n+1)}})(\boldsymbol{\varepsilon}_{(n+1)} - \boldsymbol{\varepsilon}^p_{(n)})$
if $d_t = 0$ *and* $d_{s\ell} = 0$ *and* $d_{st} = 0$ **then**
  Yield stresses: $Y_{CP}(\bar{\varepsilon}^p_{(n)})$, $Y_{TP}(\bar{\varepsilon}^p_{(n)})$ and $S_{LP}(\bar{\varepsilon}^p_{(n)})$ **Yield function Eq. (13)**: $\phi^p_{(n+1)}$
  General convex cutting-plane algorithm (return-mapping):
  $\boldsymbol{\sigma}^{(k)}_{(n+1)} = \boldsymbol{\sigma}^{tr}_{(n+1)}$
  $\phi^{p^{(k+1)}}_{(n+1)} = \phi^p_{(n+1)}$
  while $\phi^{p^{(k+1)}}_{(n+1)} > tol$ **do**
    Derivative of the plastic potential function with respect to the stress tensor: $\partial_{\boldsymbol{\sigma}^{(k)}_{(n+1)}}(\varphi^p)$
    Increment of the consistency parameter:
    $\Delta\gamma_{(n+1)} = -\frac{\phi^p_{(n+1)}}{\frac{d\phi^p_{(n+1)}}{d\gamma_{(n+1)}}}$
    Update the plastic strain tensor:
    $\boldsymbol{\varepsilon}^{p^{(k+1)}}_{(n+1)} = \boldsymbol{\varepsilon}^{p^{(k)}}_{(n+1)} + \Delta\gamma^{(k)}_{(n+1)}\partial_{\boldsymbol{\sigma}^{(k)}_{(n+1)}}(\varphi^p)$
    Update the stress tensor:
    $\boldsymbol{\sigma}^{(k+1)}_{(n+1)} = \boldsymbol{\sigma}^{(k)}_{(n+1)} - \Delta\gamma^{(k)}_{(n+1)}\mathbb{C}_e\partial_{\boldsymbol{\sigma}^{(k)}_{(n+1)}}(\varphi^p)$
    Update the equivalent plastic strain:
    $\bar{\varepsilon}^{p^{(k+1)}}_{(n+1)} = \bar{\varepsilon}^{p^{(k)}}_{(n+1)} + \Delta\gamma^{(k)}_{(n+1)}\sqrt{\frac{1}{2}}\left\|\partial_{\boldsymbol{\sigma}^{(k)}_{(n+1)}}(\varphi^p)\right\|$
    Update yield stresses: $Y_{CP}(\bar{\varepsilon}^{p^{(k+1)}}_{(n+1)})$, $Y_{TP}(\bar{\varepsilon}^{p^{(k+1)}}_{(n+1)})$ and $S_{LP}(\bar{\varepsilon}^{p^{(k+1)}}_{(n+1)})$
    Yield function Eq. (13): $\phi^{p^{(k+1)}}_{(n+1)}$
    $k = k + 1$
  end
end

References

[1] Orifici AC, Herszberg I, Thomson RS. Review of methodologies for composite material modelling incorporating failure. Compos Struct 2008;86(1–3):194–210.
[2] Schultheisz CR, Waas AM. Compressive failure of composites, part I: testing and micromechanical theories. Prog Aerosp Sci 1996;32(1):1–42.
[3] Fleck NA, Liu D. Microbuckle initiation from a patch of large amplitude fibre waviness in a composite under compression and bending. Eur J Mech A Solids 2001;20(1):23–37.
[4] Liu P, Zheng J. Recent developments on damage modeling and finite element analysis for composite laminates: A review. Mater Des 2010;31(8):3825–34.
[5] Guo Q, Yao W, Li W, Gupta N. Constitutive models for the structural analysis of composite materials for the finite element analysis: A review of recent practices. Compos Struct 2021;260:113267.
[6] Maimí P, Camanho PP, Mayugo J, Dávila C. A continuum damage model for composite laminates: Part I–Constitutive model. Mech Mater 2007;39(10):897–908.
[7] Lemaitre J. A continuous damage mechanics model for ductile fracture. 1985.
[8] Lemaitre J. A course on damage mechanics. Springer Science & Business Media; 2012.
[9] Simo JC, Ju J. Strain-and stress-based continuum damage models—I. Formulation. Int J Solids Struct 1987;23(7):821–40.
[10] Matzenmiller A, Lubliner J, Taylor R. A constitutive model for anisotropic damage in fiber-composites. Mech Mater 1995;20(2):125–52.
[11] Shahid I, Chang F-K. An accumulative damage model for tensile and shear failures of laminated composite plates. J Compos Mater 1995;29(7):926–81.
[12] Chen J, Morozov E, Shankar K. A combined elastoplastic damage model for progressive failure analysis of composite materials and structures. Compos Struct 2012;94(12):3478–89.
[13] Zenia S, Ayed LB, Nouari M, Delamézière A. Numerical prediction of the chip formation process and induced damage during the machining of carbon/epoxy composites. Int J Mech Sci 2015;90:89–101.
[14] Reinoso J, Catalanotti G, Blázquez A, Areias P, Camanho P, París F. A consistent anisotropic damage model for laminated fiber-reinforced composites using the 3D-version of the Puck failure criterion. Int J Solids Struct 2017;126:37–53.
[15] Quintanas-Corominas A, Maimí P, Casoni E, Turon A, Mayugo JA, Guillamet G, Vázquez M. A 3D transversally isotropic constitutive model for advanced composites implemented in a high performance computing code. Eur J Mech A Solids 2018;71:278–91.
[16] Din IU, Hao P, Franz G, Panier S. Elastoplastic CDM model based on puck's theory for the prediction of mechanical behavior of Fiber Reinforced Polymer (frp) composites. Compos Struct 2018;201:291–302.
[17] Chang F-K, Chang K-Y. A progressive damage model for laminated composites containing stress concentrations. J Compos Mater 1987;21(9):834–55.
[18] Chang F-K, Lessard LB. Damage tolerance of laminated composites containing an open hole and subjected to compressive loadings: Part I—Analysis. J Compos Mater 1991;25(1):2–43.
[19] Camanho P, Arteiro A, Melro A, Catalanotti G, Vogler M. Three-dimensional invariant-based failure criteria for fibre-reinforced composites. Int J Solids Struct 2015;55:92–107.
[20] Leone Jr FA. Deformation gradient tensor decomposition for representing matrix cracks in fiber-reinforced materials. Composites A 2015;76:334–41.
[21] Llobet J, Maimí P, Turon A, Bak B, Lindgaard E, Carreras L, Essa Y, de la Escalera FM. A continuum damage model for composite laminates: Part IV-Experimental and numerical tests. Mech Mater 2021;154:103686.
[22] Lapczyk I, Hurtado JA. Progressive damage modeling in fiber-reinforced materials. Composites A 2007;38(11):2333–41. http://dx.doi.org/10.1016/j.compositesa.2007.01.017, URL: https://www.sciencedirect.com/science/article/pii/S1359835X07000218, CompTest 2006.
[23] Cózar I, Otero F, Maimí P, González E, Miot S, Turon A, Camanho PP. A three-dimensional plastic-damage model for polymer composite materials. Composites A 2022;163:107198.
[24] Marsden JE, Hughes TJ. Mathematical foundations of elasticity. Courier Corporation; 1994.
[25] Simo JC, Hughes TJ. Computational inelasticity, Vol. 7. Springer Science & Business Media; 2006.
[26] Soutis C. Measurement of the static compressive strength of carbon-fibre/epoxy laminates. Compos Sci Technol 1991;42(4):373–92.
[27] Pinho S, Iannucci L, Robinson P. Physically-based failure models and criteria for laminated fibre-reinforced composites with emphasis on fibre kinking: Part I: Development. Composites A 2006;37(1):63–73.
[28] ABAQUS Inc. User's manual, 2022. Pawtucket, RI, USA; 2022.
[29] González E, Maimí P, Martín-Santos E, Soto A, Cruz P, de la Escalera FM, de Aja JS. Simulating drop-weight impact and compression after impact tests on composite laminates using conventional shell finite elements. Int J Solids Struct 2018;144:230–47.
[30] Joseph AP, Davidson P, Waas AM. Open hole and filled hole progressive damage and failure analysis of composite laminates with a countersunk hole. Compos Struct 2018;203:523–38.
[31] Tan W, Falzon BG, Chiu LN, Price M. Predicting low velocity impact damage and Compression-After-Impact (CAI) behaviour of composite laminates. Composites A 2015;71:212–26.
[32] Egan B, McCarthy M, Frizzell R, Gray P, McCarthy C. Modelling bearing failure in countersunk composite joints under quasi-static loading using 3D explicit finite element analysis. Compos Struct 2014;108:963–77.
[33] Liu P, Cheng X, Wang S, Liu S, Cheng Y. Numerical analysis of bearing failure in countersunk composite joints using 3D explicit simulation method. Compos Struct 2016;138:30–9.
[34] Nebe M, Soriano A, Braun C, Middendorf P, Walther F. Analysis on the mechanical response of composite pressure vessels during internal pressure loading: FE modeling and experimental correlation. Composites B 2021;212:108550.
[35] Camanho P, Matthews F. Delamination onset prediction in mechanically fastened joints in composite laminates. J Compos Mater 1999;33(10):906–27.
[36] Camanho PP, Maimí P, Dávila C. Prediction of size effects in notched laminates using continuum damage mechanics. Compos Sci Technol 2007;67(13):2715–27.

[37] Vogler M, Rolfes R, Camanho P. Modeling the inelastic deformation and fracture of polymer composites–Part I: plasticity model. Mech Mater 2013;59:50–64.
[38] Bessa M. Meso-mechanical model of the structural integrity of advanced composite laminates (Ph.D. thesis), University of Porto; 2010.
[39] Seon G, Makeev A, Schaefer JD, Justusson B. Measurement of interlaminar tensile strength and elastic properties of composites using open-hole compression testing and digital image correlation. Appl Sci 2019;9(13):2647.
[40] Wisnom M, Hallett S, Soutis C. Scaling effects in notched composites. J Compos Mater 2010;44(2):195–210.
[41] Catalanotti G, Camanho P, Marques A. Three-dimensional failure criteria for fiber-reinforced laminates. Compos Struct 2013;95:63–79.
[42] Gutkin R, Pinho S. Practical application of failure models to predict the response of composite structures. In: Proceedings of 18th international conference on composite materials. 2011.
[43] Soutis C, Fleck N. Static compression failure of carbon fibre T800/924c composite plate with a single hole. J Compos Mater 1990;24(5):536–58.
[44] Soutis C, Fleck N, Smith P. Failure prediction technique for compression loaded carbon fibre-epoxy laminate with open holes. J Compos Mater 1991;25(11):1476–98.
[45] Soutis C, Fleck N, Curtis P. Hole-hole interaction in carbon fibre/epoxy laminates under uniaxial compression. Composites 1991;22(1):31–8.
[46] Soutis C, Curtis P, Fleck NA. Compressive failure of notched carbon fibre composites. Proc R Soc Lond Ser A 1993;440(1909):241–56.
[47] Soutis C, Curtis P. A method for predicting the fracture toughness of CFRP laminates failing by fibre microbuckling. Composites A 2000;31(7):733–40.
[48] Ahn J, Waas AM. Prediction of compressive failure in laminated composites at room and elevated temperature. AIAA J 2002;40(2):346–58.
[49] Bouvet C, Rivallant S. Damage tolerance of composite structures under low-velocity impact. In: Dynamic deformation, damage and fracture in composite materials and structures. Elsevier; 2023, p. 3–28.
[50] Liv Y. A contribution to the understanding of compression after impact of composite laminates (Ph.D. thesis), Universitat de Girona; 2017.
[51] Sun X, Hallett S. Failure mechanisms and damage evolution of laminated composites under compression after impact (CAI): Experimental and numerical study. Composites A 2018;104:41–59.
[52] Soto A, González E, Maimí P, De La Escalera FM, De Aja JS, Alvarez E. Low velocity impact and compression after impact simulation of thin ply laminates. Composites A 2018;109:413–27.